
1 **Dynamic Response of Pile-Slab Retaining Wall Structure**
2 **under Rockfall Impact**

3 Peng Zou^{1,2,3}, Gang Luo^{1*}, Yuzhang Bi⁴, Hanhua Xu^{2,3}

4 1. *Faculty of Geosciences and Engineering, Southwest Jiaotong University, Chengdu 611756, China*

5 2. *Kunming Prospecting Design Institute of China Nonferrous Metals Industry Co., Ltd, Yunnan*
6 *650051, China*

7 3. *Yunnan Key Laboratory of Geotechnical Engineering and Geohazards, Kunming, 650051, China*

8 4. *College of Resources and Environment, Fujian Agriculture and Forestry University, Fuzhou*
9 *350002, China*

10 ***Corresponding author at:** Faculty of Geosciences and Engineering, Southwest Jiaotong
11 University, Chengdu 611756, China

12 E-mail addresses: luogang@home.swjtu.edu.cn (G. Luo).

13 **Abstract:** The pile-slab retaining wall, as an innovative rockfall protection structure, has been
14 extensively utilized in the western mountainous regions of China. With its characteristics of a small
15 footprint, high interception height, and ease of construction, this structure demonstrates promising
16 potential for application in mountainous regions worldwide, such as the Himalayas, Andes, and Alps.
17 However, its dynamic response upon impact and impact resistance energy remain ambiguous, due
18 to the intricate composite nature of the structure. To elucidate this, an exhaustive dynamic analysis
19 of a four-span pile-slab retaining wall with a cantilever section of 6 m under various impact
20 scenarios was conducted utilizing the finite element numerical simulation method. The rationality
21 of the selected material constitutive models and the numerical algorithm was validated by
22 reproducing two physical model tests. The simulation results reveal the following: (1) The lateral
23 displacement of the pile at the ground surface and the concrete damage under the pile as the impact
24 center is greater than those under the slab as the impact center, implying that the impact location
25 has a significant influence on the stability of the structure. (2) There is a positive correlation between
26 the response indexes (impact force, interaction force, lateral deformation of pile and slab, concrete
27 damage) and the impact velocities. (3) The rockfall peak impact force, the ratio of peak impact force
28 to peak interaction force, and lateral displacement of pile at the ground surface had strong linear
29 relationships with rockfall energy. (4) Relative to the bending moment, shear force and damage
30 degree, the lateral displacement of pile at the ground surface is the first to reach its limit value.
31 Taking the lateral displacement of the pile at the ground surface as the controlling factor, the
32 estimated maximum impact energy that the pile-slab retaining wall can withstand is 905 kJ in this
33 study when the structure top is taken as the impact point. In cases where the impact energy of falling
34 rocks exceeds 905 kJ, it is recommended to optimize the mechanical properties of the cushion layer,
35 improve the elastic modulus of concrete, increase the reinforcement ratio of longitudinal tension
36 bars, enlarge the section size of pile at ground level, or add anchoring measures to enhance the
37 bending resistance of the retaining structure.

38 **Keywords:** rockfall, pile-slab retaining wall, numerical simulation, dynamic response

39 **List of symbols**

P	Actual lateral soil resistance (kPa).	F_{dm}	Peak impact force (kN).
P_u	Ultimate lateral soil resistance (kPa).	F_{im}	Peak interaction force (kN).
S_{u_cu}	Consolidated isotropic undrained tri-axial shear strength of soil (kPa/m).	α	Ratio of the peak impact force to the peak interaction force (%).
y	Actual lateral soil deformation (m).	S_{mpt}	Maximum lateral displacement of pile at the ground surface (mm).
B	Pile width (m).	N_d	Number of damage failure units.
z	Depth below the ground surface (m).	β	Ratio of damage failure units to overall structure units (%).
S_p	Shape correction factor of pile section.	m	Impactor mass (kg).
E	Initial kinetic energy of impactor.	v	Initial velocity of impactor (m/s).

40 **1. Introduction**

41 Rockfall disasters pose a great threat to roads, railways, buildings and inhabitants in
42 mountainous terrain (Hungri et al., 2014; Crosta and Agliardi, 2004; Shen et al., 2019). It can be
43 described as a process that the rapid bouncing, rolling and sliding movement of one (or several)
44 boulders down a slope (Peila and Ronco, 2009). Muraishi et al. (2005) surveyed 607 rockfall
45 events and found that about 68% of rockfall events have an impact energy of less than 100 kJ,
46 whereas 90% have less than 1000 kJ. Chau et al. (2002) indicated that the rotational kinetic energy
47 of rockfall only accounts for 10% of the total kinetic energy. To mitigate such geological hazards,
48 scholars and engineers have proposed different types of technical solutions. Two primary categories
49 of defensive measures are commonly employed: active and passive. Active protection measures
50 mainly include masonry protection, reinforcement protection (grouting, anchor rod, and anchor
51 cable), initiative protective net (Yang et al., 2019). Passive protection measures include passive
52 flexible protection (Yu et al., 2021), rockfall shed gallery (Zhao et al., 2018), rockfall retaining wall.
53 Considering many factors, such as technological feasibility and economic considerations, rockfall
54 retaining wall is frequently employed in practical engineering (Volkwein et al., 2011).

55 Currently, various types of retaining walls are utilized in engineering projects aimed at
56 intercepting falling boulders. These include masonry retaining walls, reinforced concrete (RC)
57 retaining walls, reinforced soil retaining walls, and pile-slab retaining walls (PSRW). Due to
58 inherent structural weakness of these walls, their ability to absorb the impact energy from rockfall

59 is limited (Mavrouli et al., 2017). To enhance the impact resistance, the reinforced concrete retaining
60 walls have been utilized (Yong et al., 2020). These structures can intercept rockfall impact energy
61 ranging approximately from 120 to 500 kJ (Maegawa et al., 2011). To prevent concrete from being
62 damaged by the direct impact of rockfall, a buffer layer is generally added in front of the structure
63 for protection, such as reinforced soil and gabion cushion (Perera et al., 2021). Although the impact
64 resistance of the structure has been improved, there is still a problem of limited interception height.
65 When the required interception height is large, the foundation size has to be increased to prevent the
66 structures from overturning. In order to mitigate against rockfall events involving higher energy
67 levels, numerous researchers have proposed the implementation of reinforced soil retaining walls.
68 Extensive studies have been conducted in this regard, demonstrating that the structures can
69 effectively intercept rockfall impact energies exceeding 5000 kJ (Lambert et al., 2009). Moreover,
70 geosynthetic have proven to be efficacious in reducing wall stresses (Lu et al., 2021). However, the
71 structure requires a substantial spatial footprint and poses an overturning risk during construction in
72 steep terrain (Peila et al., 2007). Additionally, when the topography at the wall site features steep
73 slopes, the available space behind the wall for accommodating rockfalls becomes constrained.

74 In response to the challenges posed by steep terrains, narrow site conditions, and suboptimal
75 foundation conditions in mountainous terrain, Hu et al. (2019) introduced the PSRW structure. This
76 structure comprises a buffer layer and an anti-slide pile-slab system, which has found widespread
77 application in southwestern China (Fig. 1). Due to the use of pile foundations, this structure exhibits
78 characteristics such as a small footprint, high interception height, and ease of construction.



79
80 **Fig. 1. PSRW in south-western China (a) Kongyu town (b) Jiuzhaigou nature reserve (c) Zhenjiangguan**
81 **tunnel exit in Chengdu-lanzhou railway (d) Zhangmu town**

82 However, the current PSRW design verification approach treats the structure as either an

83 underground continuous wall (CAGHP, 2019) or an elastic cantilever beam (Tian et al., 2024). The
84 structural design primarily considers the impact force of falling rocks as the sole external
85 influencing parameter, while the impact energy is seldom taken into account. Furthermore, existing
86 research primarily focuses on single slabs and piles impacted by rockfall (Wu et al., 2021; Yong et
87 al., 2021). Consequently, due to the scarcity of comprehensive research reports on the ultimate load-
88 bearing capacity of this structure, it is frequently overlooked during the initial selection of protective
89 structures, and potential failure scenarios may be underestimated (Fig. 2). Additionally, because of
90 the composite nature of this structure, the dynamical response at various impact points remains
91 elusive.



Fig. 2. Some PSRW in Zhangmu Town were damaged by falling rocks.

92 Therefore, determining the maximum impact energy, analyzing the structural dynamic
93 response, and assessing concrete damage are crucial factors in determining the effectiveness of the
94 structure in mitigating rockfall hazards. Based on the unique advantages of the finite element
95 method, this study employs the LS-DYNA to simulate the complete process of rockfall impacting
96 on PSRW. This methodology has been widely adopted by numerous researchers and demonstrated
97 as suitable for simulating impact problems of reinforced concrete structure (Zhong et al., 2022; Fan
98 et al., 2022; Bi et al., 2023). In conclusion, a full-scale numerical model of a four-span pile-slab
99 retaining wall satisfying specification requirements is established. The rationality of the selected
100 material constitutive models and a numerical algorithm was validated by reproducing two physical
101 model tests. The structure's dynamic behavior under different impact velocities and impact centers

102 is discussed (Fig. 3). The results provide insights into structure dynamic response analysis of the
103 PSRW and serve as a benchmark for further research.

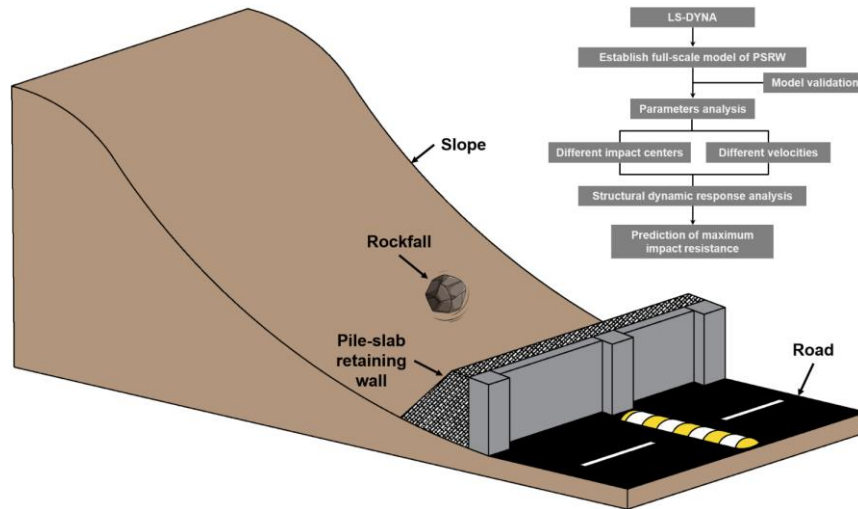


Fig. 3 Mind mapping.

104 2. Numerical model and validations

105 2.1. Model configuration

106 2.1.1. Engineering background

107 The design drawing of the PSRW (Fig. 4) is consistent with the actual project located in
108 Zhangmu Town, China. Given the large scale of the actual engineering structure, numerical
109 simulations have been focused solely on a representative four-span structure, incorporating
110 appropriately simplified boundary conditions to facilitate the analysis. For a comprehensive
111 understanding of the modeling specifics, kindly refer to Section 2.1.3. The anti-slide piles with a
112 concrete protective layer thickness of 0.04 m have a cross-section area of $1.8 \text{ m} \times 1.25 \text{ m}$. The total
113 pile length is 12 m, and the embedded section is 6 m. The HRB 400 longitudinal bar with diameters
114 of 25 mm and 32 mm were arranged in the pile (Fig. 4c). The stirrups are HRB335 with a diameter
115 of 16 mm and a spacing of 200 mm. The slabs between the piles are 6 m in length, 3.5 m in width,
116 and 0.5 m in thickness. These slabs contain two layers of 16 mm-diameter reinforced bar. The sand
117 buffer layer are 1 m and 5 m on top and bottom, respectively. A geogrid is horizontally placed in the
118 buffer layer at 0.25 m intervals. Lastly, 1 m^3 sphere rock boulder with a diameter of 1.24 m was set
119 as an impactor. The impact locations are 2# slab center (CS) and 3# pile center (CP) at 5.25 m over
120 the ground.

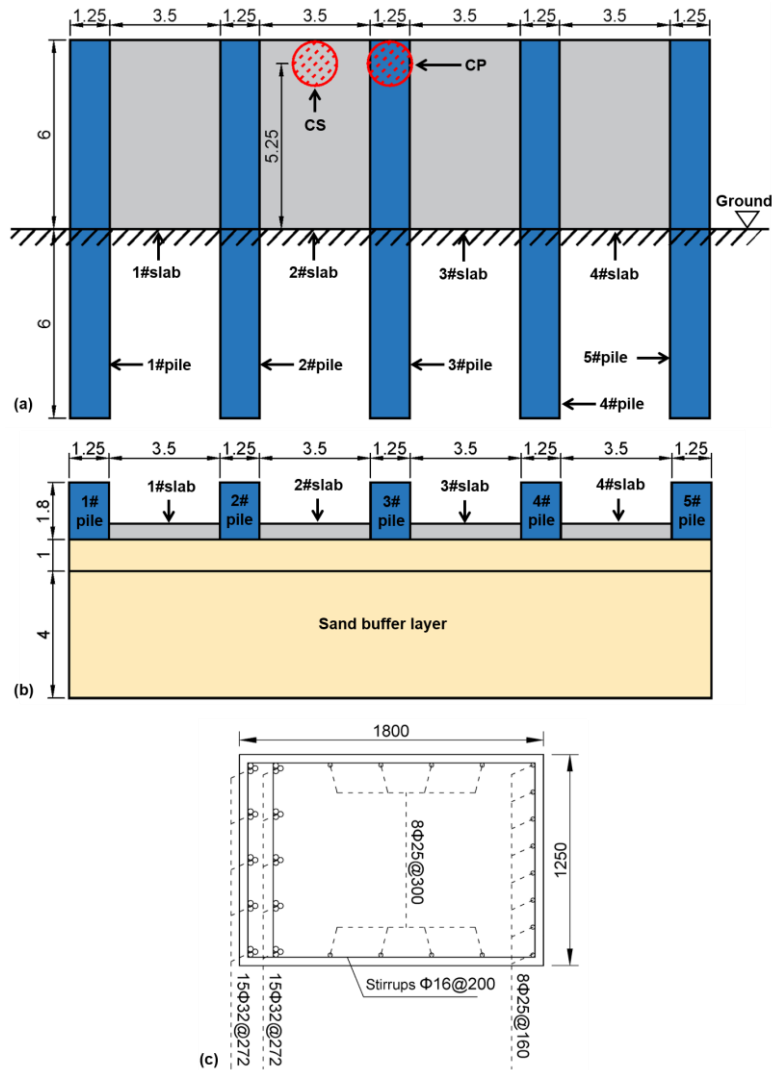


Fig. 4. The design diagram of PSRW (a) front view (unit: m) (b) top view (unit: m) (c) cross-section profile of pile (unit: mm).

121 2.1.2. Soil-pile interaction

122 Under the impacting, the lateral deformations of the pile are greatly influenced by the plastic
 123 behavior of the soil, particularly the soil near the pile. Given their importance and complexity, it
 124 isn't easy to thoroughly describe soil-pile interactions. This paper calculates the pile-soil interaction
 125 by the lateral resistance-deflection (p - y) curve method. As state by Truong and Lehane (2018), the
 126 p - y curves for square cross-section pile are utilized as

127
$$\frac{P}{P_u} = \tanh \left[5.45 \left(\frac{y}{B} \right)^{0.52} \right] \quad (1)$$

128
$$\frac{P}{S_{u_cu}} = 10.5 \left[1 - 0.75e^{-0.6z/B} \right] S_p \quad (2)$$

129 where P is the actual lateral soil resistance, kPa; P_u is the ultimate lateral soil resistance, kPa;
130 S_{u_cu} is consolidated isotropic undrained triaxial shear strength of soil, kPa/m; y is the actual lateral
131 soil deformation, m; B is pile width, m; z is depth below the soil surface, m; S_p is a shape correction
132 factor.

133 According to the reference and simulated model, the S_{u_cu} and S_p are adopted as 1.5 kPa/m and
134 1.25, respectively. Besides, the soil is modeled by compressive inelastic springs, arranged every
135 0.25 m along the pile height and side (Fig. 5a).

136 2.1.3. Numerical model and numerical simulation scheme

137 (1) Numerical model

138 The numerical model of PSRW is shown in Fig. 5. The material constitutive models, unit types,
139 physical-mechanical parameters, and parameter source for all components are listed in Table 1. The
140 rationality of all material constitutive models and physical mechanics parameters were verified in
141 Section 2.2. The bottom of piles and buffer layers are fixed for the boundary conditions. Additionally,
142 both sides of the buffer layer are blocked by infinitely rigid walls. The contact type between the
143 rockfall, sand buffer layer, and pile-slab structure was set to automatic surface-to-surface.

144 (2) Numerical simulation scheme

145 According to previous research (Muraishi et al., 2005; Chau et al., 2002), angular velocity of
146 impactor was neglected in numerical simulations, and line velocities were set as 10, 15, 20, 25, and
147 30 m/s, corresponding to impact energies of 130, 292.5, 520, 812.5, and 1170 kJ (

148 Table 2). The linear velocity is perpendicular to surface of the buffer layer.

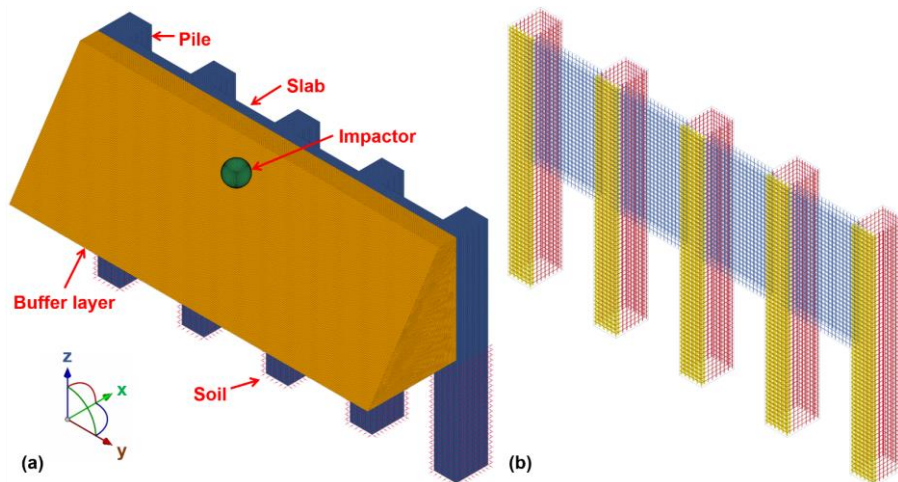


Fig. 5. Numerical model of the PSRW (a) numerical model (b) reinforced bar of PSRW (unit: mm).

149

Table 1 Material constitutive model and physical-mechanical parameters for various components of PSRW.

Items	Constrained model	Unit types	Integral methods	Density (kg/m ³)	Young's modul (MPa)	Poisson's ratio
Concrete	Continue cap concrete (MAT_159) (Heng et al., 2021)	Solid element	One integration point	2450	30000	0.3
Reinforced bar	Plastic kinematic model (MAT_003) (Heng et al., 2021)	Beam element	2×2 Gauss integration	7850	204000	0.3
Sand buffer layer	Soil-foam model (MAT_063) (Bhatti and Kishi, 2010)	Solid element	One integration point	1720	100	0.3
Impactor	Rigid body (MAT_020)	Solid element	One integration point	2600	20000	0.25
Geogrid	Plastic kinematic model (MAT_003) (Lee et al., 2010)	Shell element	Belytschko-Tsay integration	1030	464	0.3

150

151

Table 2 Detailed numerical simulation scheme.

Case	Impact location	Impact height (m)	Impact velocity (m/s)	Impact kinetic energy (kJ)
CP-V10	3# pile center	5.25	10	130
CP-V15			15	292.5
CP-V20			20	520
CP-V25			25	812.5
CP-V30			30	1170
CS-V10	2# slab center	5.25	10	130
CS-V15			15	292.5
CS-V20			20	520
CS-V25			25	812.5
CS-V30			30	1170

152

Note: CP denotes the 3# pile center as impact location; CP denotes the 2# slab center as impact location; V denotes the velocities of rockfall.

153

154 2.2. Model validation

155

In order to verify the rationality of the selected material constitutive model and the established numerical model. Two physical model tests from previously published papers (Heng et al., 2021; Demartino et al., 2017; Schellenberg, 2008) were selected to reproduce.

156

157

158

2.2.1. Failure test of RC cantilever column

159

The physical model test conducted by Demartino et al. (2017) was selected to verify the ability of constitutive model to reflect the accumulative damage for RC structures under impact loads. The model is composed of a cylindrical column with a diameter of 0.3 m and a height of 1.7 m, and a square-section concrete foundation with length of 0.9 m and height of 0.5 m. The column was reinforced with sixteen 8 mm diameter longitudinal reinforced bar and 6.5 mm diameter stirrups at 100 mm spacing. The foundation was firmly connected to the ground using four 50 mm diameter high-strength prestressed reinforced bar. The experiment involved a test truck made of Q235 steel (considered as a rigid body) (Fig. 6a). The impactor was positioned 0.4 m above the bottom of the

166

167 column and was released at a velocity of 3.02 m/s (impact energy of 7.21 kJ). Fig. 6b shows the
 168 numerical model with hexahedral mesh. The material constitutive models for components are shown
 169 in Table 1. For the boundary conditions, the model was fixed with four high-strength bolts. The trend
 170 and amplitude of the impact forces by numerical simulations closely matched the experimental
 171 results (Fig. 7). The deviations of peak impact forces between the numerical simulations and the
 172 experiments were below 10% (Table 3). Similarly, Table 4 indicates a consistency between the
 173 extent of the experimental and numerical damage in concrete. These results suggest that the
 174 numerical model and its governing parameters can reliably simulate the accumulative damage in
 175 RC structures subjected to impact loads. Considering both accuracy and computational time, a mesh
 176 size of 50 mm was selected for the numerical simulations conducted in this study.

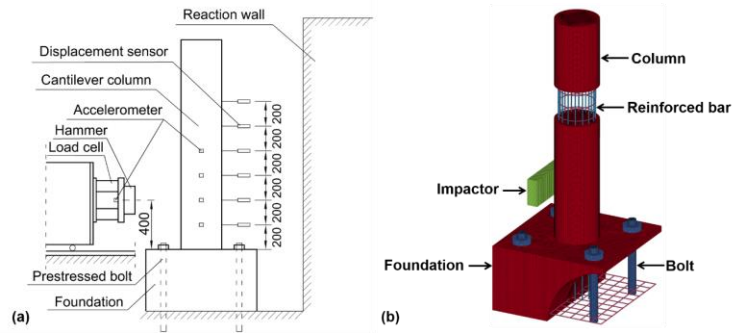


Fig. 6. Model of RC cantilever column failure test
(a) experimental model (b) numerical model (unit: mm).

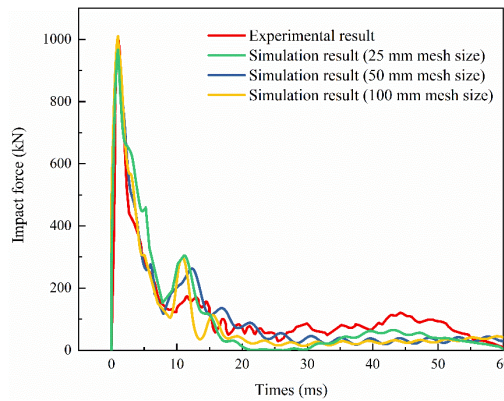


Fig. 7. Dynamic curve of impact force with different mesh size.

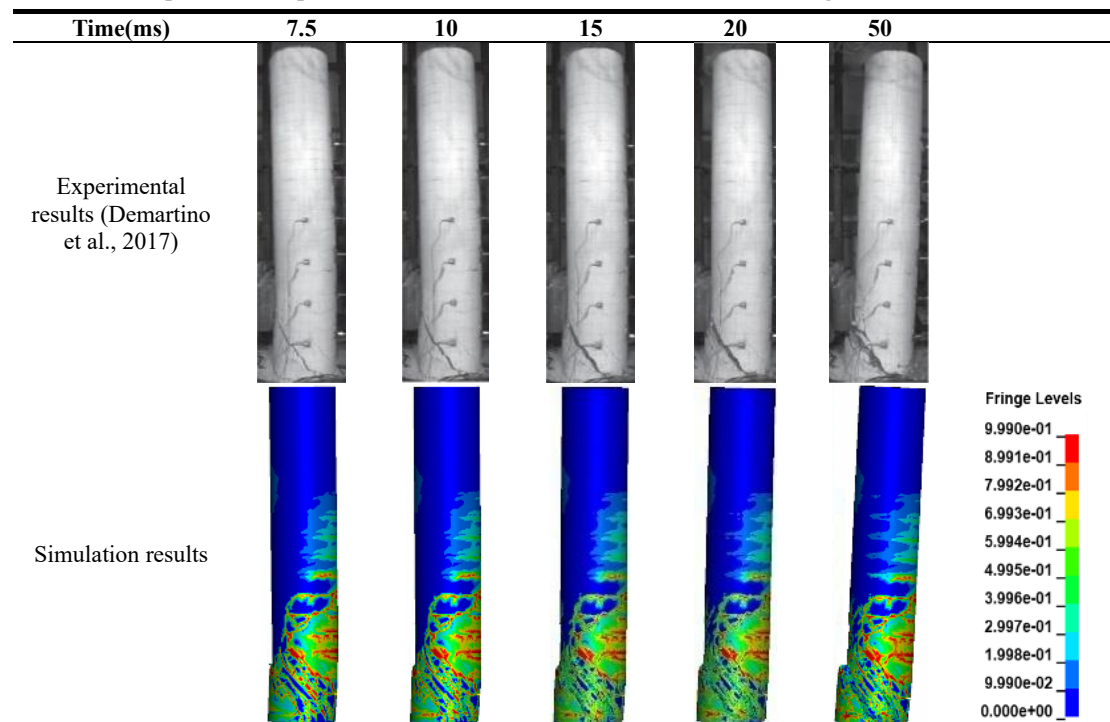
177

178

Table 3 Simulation results of different mesh sizes.

Items	Impact force (kN)	Displacement of column at 1.2m height (mm)	Number of the element	Computational time (hour)
Physical model test	999.52	22.3	/	/
25 mm mesh size	966.72	23.1	5462900	24
50 mm mesh size	978.1	22	807534	4.2
100 mm mesh size	1009.35	21.3	172268	1.2

Table 4 Comparison of experimental and simulation results of concrete damage accumulation with time.



180 2.2.2. Failure test of RC slab with a buffer layer

181 The physical model test conducted by Schellenberg (2008) was selected to validate the
 182 capability of the constitutive model to reflect the interaction among the boulder, sand buffer layer,
 183 and RC structure. The specimen comprises a RC slab measuring $1.5 \text{ m} \times 1.5 \text{ m} \times 0.23 \text{ m}$ and a sand
 184 buffer layer with 0.5 m in radius and 0.45 m in thickness (Fig. 8). The slab is reinforced with one
 185 layer of reinforced bar with 12 mm diameter and a spacing of 95 mm for the lower layer. The
 186 diameter and density of the boulder are 0.8 m and 3110 kg/m^3 , respectively. The impact position is
 187 located at the center of the buffer layer, with an impact velocity of 5.5 m/s (impact energy of 14.4
 188 kJ). The material constitutive models for concrete, reinforced bar, and sand buffer layer are shown
 189 in Table 1. For the boundary conditions, the bottom of the supports was fixed.

190 Fig. 9 presents the dynamic curve of impact force, displacement of slab center, and axial strain
 191 of center reinforced bar. The results demonstrate that the deviations of the peak impact force, the
 192 maximum strain of reinforced bar, and the slab center displacement are less than 10% . Therefore,
 193 the numerical model and its governing parameters are deemed reliable for simulating the behavior
 194 of a sand cushion layer and an RC structure under impact loads.

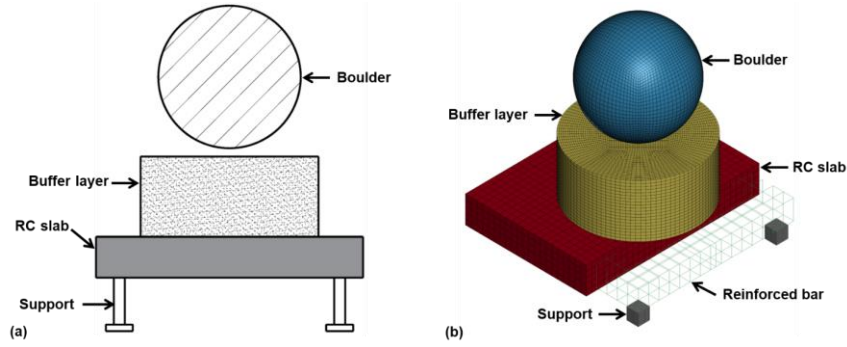


Fig. 8. Model of RC slab failure test
(a) experimental model (b) numerical model (unit: mm).

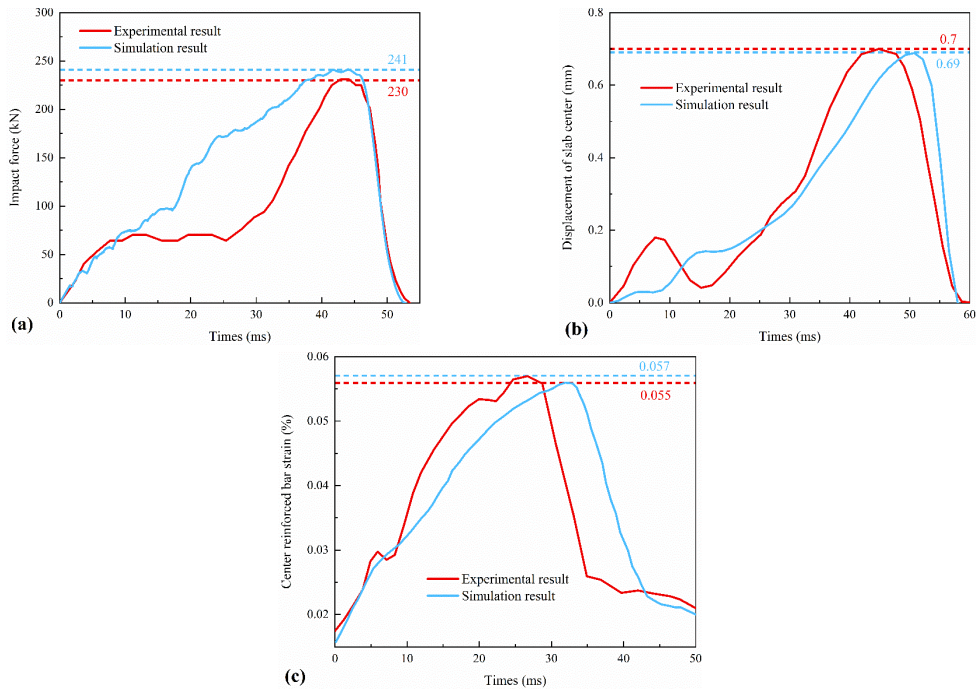


Fig. 9. Comparisons between experimental and simulation results
(a) impact force (b) displacement of slab center (c) axial strain of reinforced bar.

195 3. Numerical results

196 In this section, the dynamic response of PSRW under different impact centers and different
 197 impact velocities are compared and analyzed. The main evaluation indexes are as follows: impact
 198 force (the contact force between the impactor and the buffer layer), interaction force (the contact
 199 force between the buffer layer and the RC structure), stress of concrete and reinforced bar, concrete
 200 damage, lateral displacement at the crown of different components (piles and slabs), and lateral
 201 displacement of all piles at the ground surface.

202 3.1. Influence of different impact centers

203 To analyze the influence of dynamic behaviors of PSRW under different impact centers, two

204 group simulations under maximum impact energy (CP-V30 and CS-V30) are selected for
 205 comparison.

206 *3.1.1. Impact force and interaction force*

207 Fig. 10a and 9b show the dynamic curves of the impact force and interaction force, respectively.
 208 Both force curves exhibit a distinct single-peaked pattern. The impact force rapidly reduces to zero
 209 due to the energy-dissipating properties of the sand buffer layer (Fig. 10a). In contrast, the
 210 interaction force remains at a non-zero value (475 kN) (Fig. 10b). Owing to the permanent
 211 deformation sustained by the structure, and the gravitational force exerted by the sand buffer acts
 212 on the surface of the structure. Furthermore, Fig. 10a illustrates the close overlap of the impact
 213 forces for various impact centers, depending on the buffer and impactor characteristics, and
 214 minimally affected by the impact center. The slight differences observed in the dynamic curve of
 215 interaction force under CP-V30 and CS-V30 may be attributed to the flexural stiffness of the slab
 216 and pile.

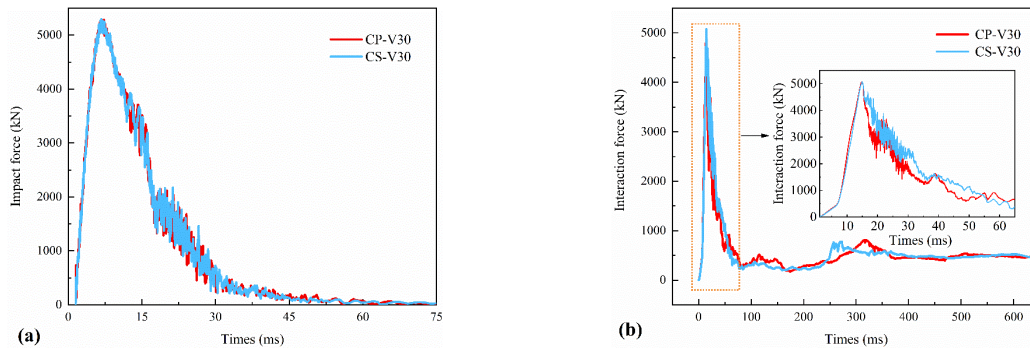


Fig. 10. Dynamic curves of impact force and interaction force under various impact centers
 (a) impact force (b) interactional force.

217 *3.1.2. Stress of concrete*

218 The minimum principal stress of concrete and the effective stress of reinforced bar are
 219 important indexes to evaluate the dynamic response of RC structures (Zhong et al., 2021; Zhong et
 220 al., 2022). Fig. 11 shows the minimum principal stress nephogram of concrete under CP-V30 from
 221 1 to 650 ms. When $t = 1$ ms (Fig. 11a), the minimum stress focus on the bottom of the piles. When
 222 $t = 14.7$ ms (Fig. 11b), the minimum principal stress of concrete around the impact point increased
 223 rapidly to 7.421 MPa. When $t = 22.8$ ms (Fig. 11c), the concrete elements at the joints of the 3# pile
 224 and slabs achieve compressive strength, leading to concrete damage. When $t = 650$ ms (Fig. 11d),
 225 the total volume of damaged elements reaches 0.63 m^3 , which occupies a proportion of 0.35%.

226 Fig. 12 shows the minimum principal stress nephogram of concrete under CP-V30 from 1 to

227 650 ms. When $t = 1$ ms, the maximum stress focus on the bottom of the piles (Fig. 12a). When $t =$
 228 14.7 ms, the minimum principal stress around the impact point increased rapidly to 12.117 MPa
 229 (Fig. 12b). When $t = 22.4$ ms, the elements of the concrete at the impact point of the 2# slab achieve
 230 ultimate compressive strength, leading to the concrete damage (Fig. 12c). When $t = 650$ ms, the total
 231 volume of damage elements reaches 0.61 m^3 (Fig. 12d), which occupies a proportion of 0.34%.

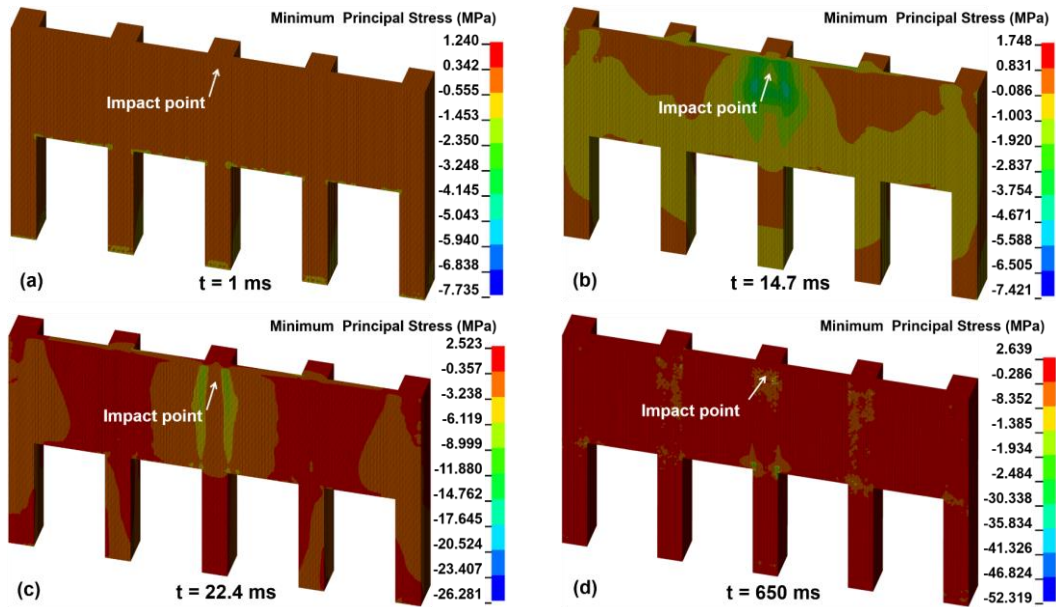


Fig. 11. Minimum principal stress nephogram of concrete under CP-V30.

232

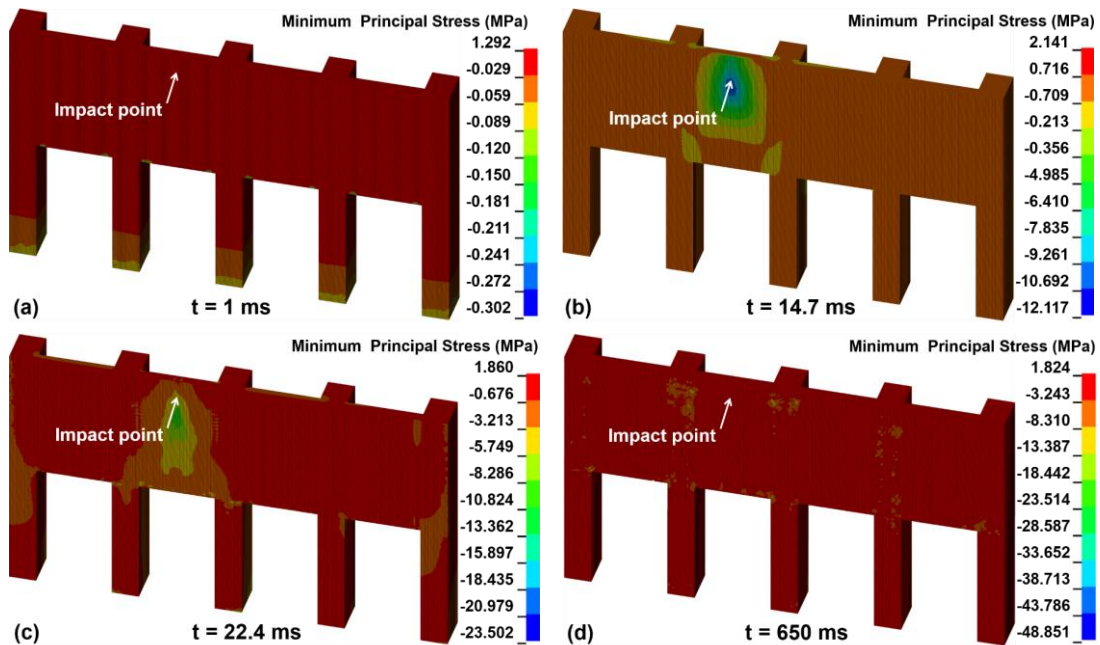


Fig. 12. Minimum principal stress nephogram of concrete under CS-V30.

233 3.1.3. *Stress of reinforced bar*

234 Fig. 13 shows the effective stress nephogram of the reinforced bar from 1 to 650 ms under the

235 condition of CP-V30. It can be observed that: (i) when $t = 1$ ms, the maximum stress concentrated
 236 at the bottom of the pile (Fig. 13a); (ii) when $t = 14.7$ ms (the moment of attaining the maximum
 237 interaction force), the maximum stress concentrated at the vicinity of the impact point and the joints
 238 of piles and slabs (Fig. 13c); (iii) when $t = 650$ ms, the maximum stress concentrated at the
 239 longitudinal bar of 2#, 3#, and 4# pile (Fig. 13d). Noteworthy, the effective stress of reinforced bar
 240 did not exceed the ultimate yield stress.

241 Fig. 14 shows the effective stress nephogram of reinforced bar from 1 to 650 ms under CS-
 242 V30. It can be observed that: (i) when $t = 1$ ms, the maximum stress concentrated at the bottom of
 243 the pile (Fig. 14a); (ii) when $t = 14.7$ ms, the effective stress of reinforced bar around the impact
 244 point increased rapidly to 137.2 MPa (Fig. 14c); (iii) when $t = 650$ ms, the maximum stress
 245 concentrated at the longitudinal bar of 2#, 3#, and 4# pile (Fig. 14d). Noteworthy, the effective
 246 stress of reinforced bar did not exceed the ultimate yield stress.

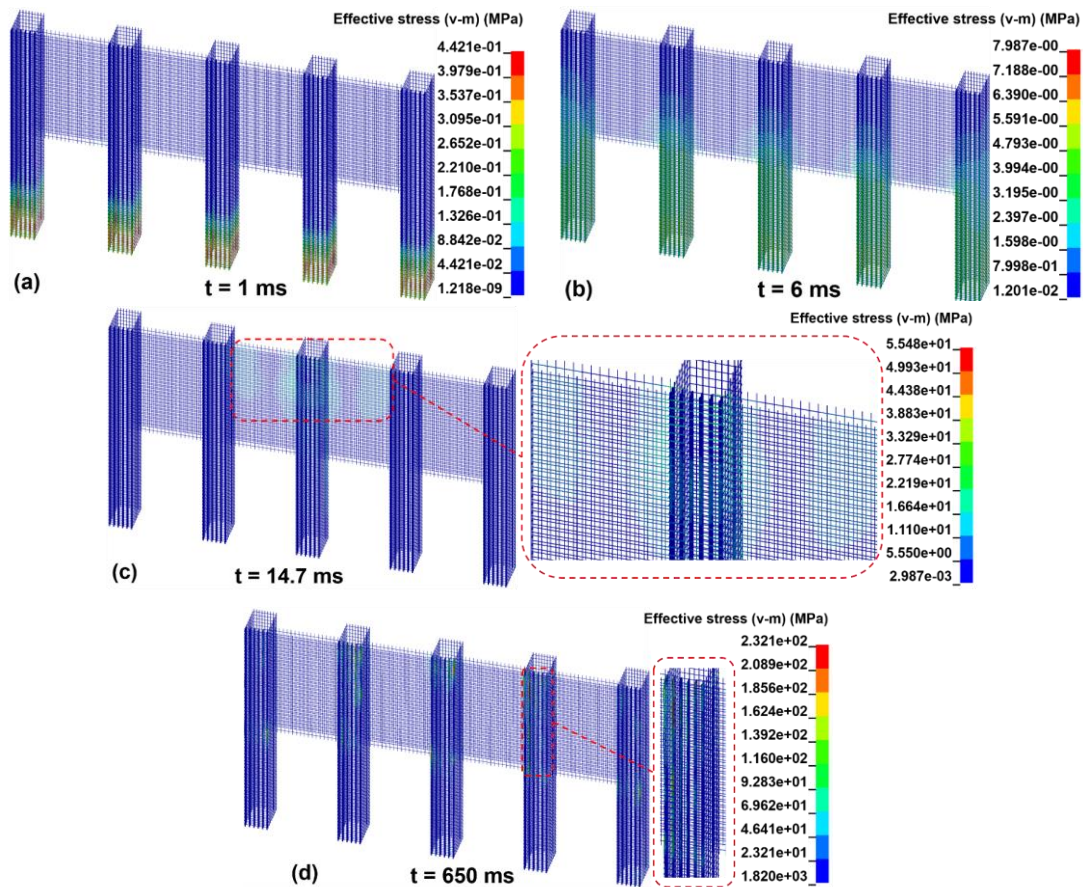


Fig. 13. Effective stress nephogram of reinforced bar under CP-V30.

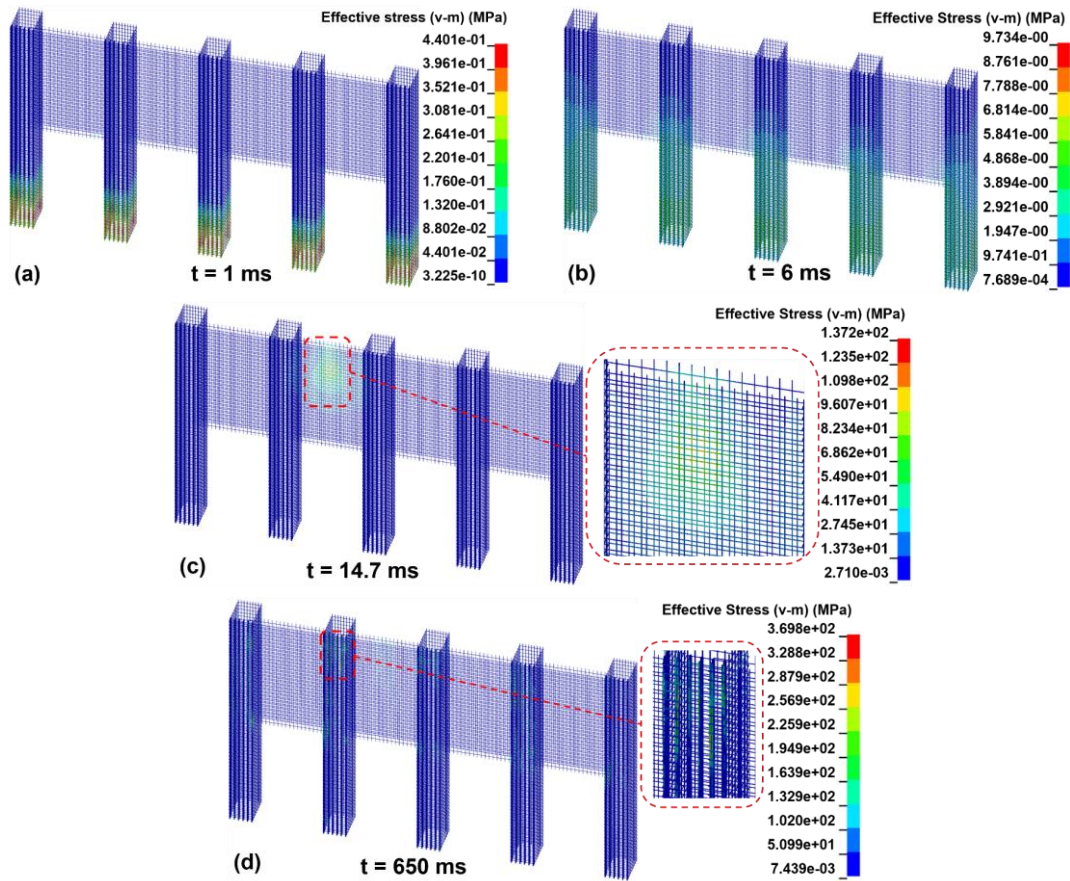


Fig. 14. Effective stress nephogram of reinforced bar under CS-V30.

247 3.1.4. Lateral displacement at the crown of different components

248 Fig. 15a presents lateral displacements at the crown of different components under CP-V30
 249 and CS-V30 conditions. The lateral displacement rapidly increased till $t = 177$ ms and gradually
 250 decreased until $t = 650$ ms. The final displacement does not reach 0, indicating plastic deformation
 251 of both the pile and the slab. Comparing the lateral displacement under CS-V30 and CP-V30 (Fig.
 252 15), the trends are consistent, but the magnitude differs. This discrepancy in magnitude can be
 253 attributed to the greater deformation capacity of slab compared to pile when subjected to the same
 254 impact energy.

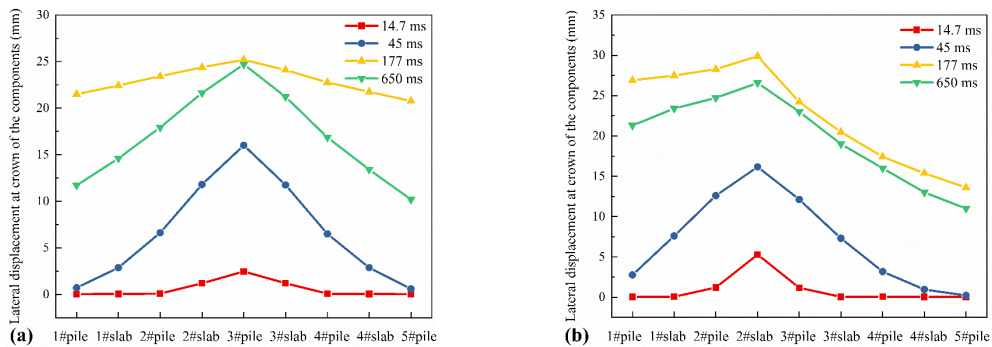
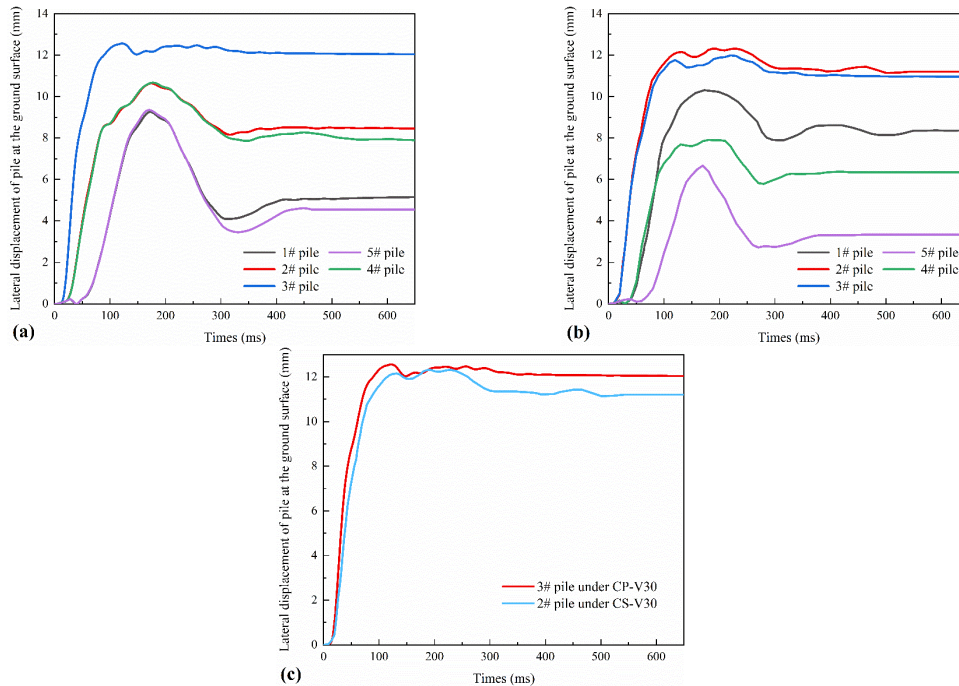


Fig. 15. Lateral displacement at crown of the components (a) CP-V30 (b) CS-V30.

255 3.1.5. Lateral displacement of piles at the ground surface

256 Fig. 16a and 16b show the dynamic curve of lateral displacement of all piles at the ground
257 surface under CP-V30 and CS-V30, respectively. Under CP-V30, the 3# pile exhibited the
258 maximum lateral displacement, whereas the 2# pile exhibited the maximum lateral displacement
259 under CS-V30. This discrepancy is due to the structural asymmetry on either side of the impact
260 center under CS-V30, which allows one side of pile #2 greater freedom, resulting in larger lateral
261 displacement. When comparing the lateral displacement of 2# pile under CS-V30 and 3# pile under
262 CP-V30 (Fig. 16c), it is apparent that the maximum lateral displacement of pile at the ground surface
263 is greater under CP conditions, despite the same impact velocity. The characteristics of the lateral
264 displacements suggest that the concrete slab is capable of undergoing larger deformations and
265 absorbing more energy.



**Fig. 16. Dynamic curves of lateral displacement of pile at the ground surface
(a) CP-V30 (b) CS-V30 (c) compare between CP-V30 and CS-V30.**

266 3.2. Influence of different impact velocities

267 Figure 17 demonstrates that under CP conditions, the impact force, interaction force, and lateral
268 displacement of pile #3 at the ground surface increase as the impact velocity of rockfall rises. When
269 the velocity increases from 15 m/s to 30 m/s, the impact force increases by 1.42, 1.91, and 2.41
270 times, the interaction force increases by 1.25, 1.47, and 1.68 times, and the lateral displacement of
271 3# pile at ground surface increases by 1.57, 2.24, and 3 times at $t = 650$ ms. By comparing the

272 magnitude of changes, the lateral displacement is more sensitive to velocity variations than impact
 273 force and structural interaction force.

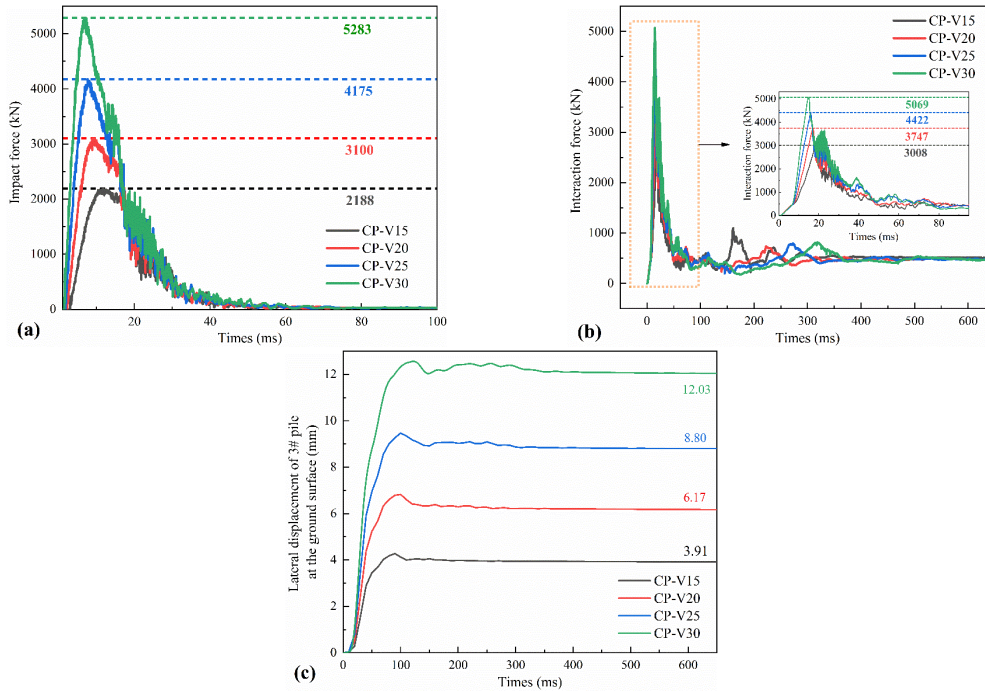
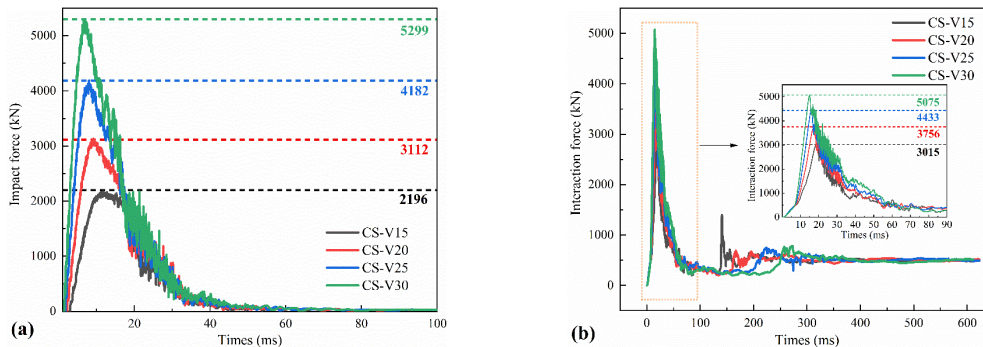


Fig. 17. Dynamic curves of evaluation indexes under various velocities
 (a) impact force (b) interactional force (c) lateral displacement at the ground surface of 3# pile.

274 Fig. 18 shows the impact force, interaction force, and lateral displacement of 2# pile at the
 275 ground surface enlarge as the impact velocity increases under CS conditions. When the velocity
 276 increases from 15 m/s to 30 m/s, the impact force increases by 1.41, 1.90, and 2.41 times, the
 277 interaction force increases by 1.24, 1.47, and 1.68 times, and the lateral displacement of 3# pile at
 278 ground surface increases by 1.55, 2.23, and 3 times at $t = 650$ ms. Similar to the CP conditions, the
 279 lateral displacement is still most sensitive to velocity variations.



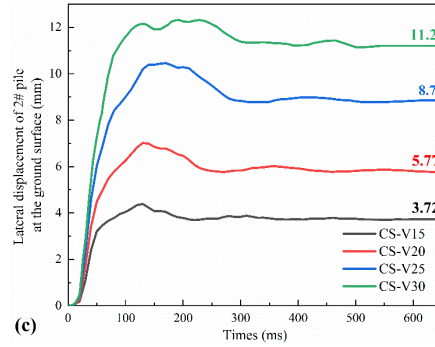


Fig. 18. Dynamic curves of evaluation indexes under various velocities
 (a) impact force (b) interactional force (c) lateral displacement at the ground surface of 3# pile.

280 **4. Discussions**

281 *4.1. Comparison of impact force calculation models*

282 A comparative analysis compared the elastic theories proposed by Labiouse et al. (1996),
 283 Kawahara and Muro (2006), Pichler et al. (2006), and Hertz (1881) was conducted to assess the
 284 validity of the numerical simulation (Fig. 19). The results reveal a fundamental linear correlation
 285 between impact force and velocity. Overall, the computational results are consistent with those of
 286 other models in terms of magnitude, thus confirming the validity of the calculations reported here.

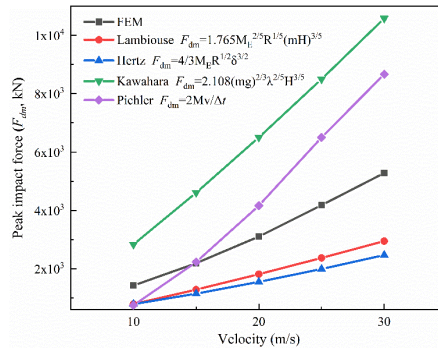


Fig. 19. Relationship between impact velocity and impact force.

287 *4.2. Relationship between structural evaluation indexes and impact energy*

288 Table 5 lists the initial kinetic energy of impactor (E), the peak impact force (F_{dm}), the peak
 289 interaction force (F_{im}), the ratio of the peak impact force to the peak interaction force (α), the
 290 maximum the lateral displacement of pile at the ground surface at $t = 650$ ms (S_{mpt}), the number of
 291 damage failure units (N_d), and the ratio of damage failure units to overall RC structure units (β).

Table 5 Simulation results of various impact cases.

Case	E (kJ)	F_{dm} (kN)	F_{im} (kN)	α (%)	S_{mpt} (mm)	N_d	β (%)
CP-V10	130	1420	2170	65.4	2.25	83	0.0059
CP-V15	292.5	2188	3008	72.7	3.91	817	0.0577
CP-V20	520	3100	3747	82.7	6.17	2179	0.1539
CP-V25	812.5	4175	4422	94.4	8.8	3088	0.2181
CP-V30	1170	5283	5069	104.2	12.03	5040	0.3559

CS-V10	130	1426	2182	65.4	1.76	52	0.0037
CS-V15	292.5	2196	3015	72.7	3.72	321	0.0227
CS-V20	520	3112	3756	82.7	5.77	1062	0.0750
CS-V25	812.5	4182	4433	94.4	8.7	2728	0.1927
CS-V30	1170	5299	5075	104.2	11.2	4880	0.3446

293 Under the premise of known impact energy, estimating impact force, interaction force, and
 294 displacement of pile for the structural design is very important. As shown in Table 5, the variation
 295 in peak impact force (F_{dm}) with different impact centers is minimal. Consequently, CP simulation
 296 results were chosen for further analysis. The dependence of the peak impact force on the impact
 297 energy is shown in Fig. 20a, with a correlation coefficient $R^2 = 0.99$, i.e.,

$$298 \quad F_{dm} = 3.69(E + 290.33) = 1845(mv^2 + 0.58) \quad (1)$$

299 where m is the impactor mass ($m = 2600$ kg herein); v is the initial impact velocity (10 m/s \leq
 300 $v \leq 30$ m/s herein).

301 The dependence of the ratio of peak impact force to peak interaction force on the impact energy
 302 is shown in Fig. 20b, with a correlation coefficient of 0.99, i.e.,

$$303 \quad \alpha = 0.037(E + 1671.89) = 18.5(mv^2 + 3.34) \quad (2)$$

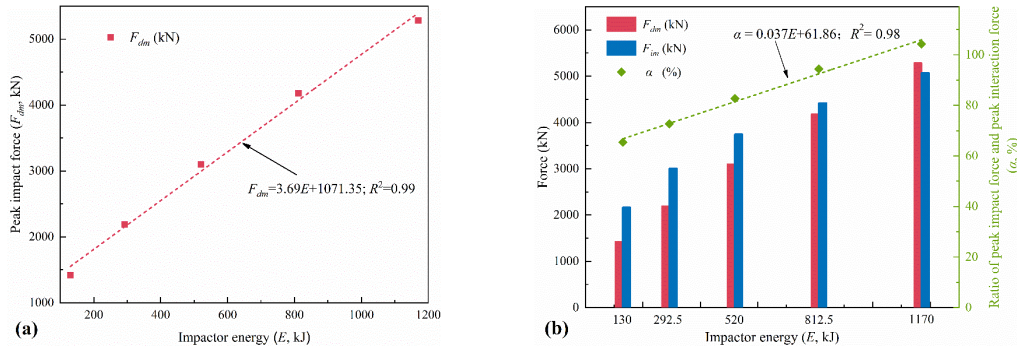


Fig. 20. Dependence of various indexes on impactor energy (a) peak impact force (b) the ratio of peak impact force and peak interaction force.

304 The lateral displacement of pile at the ground surface is an important index to judge the failure
 305 of pile foundation under lateral load. As shown in Table 5, the maximum lateral displacement of
 306 pile at the ground surface under pile as impact center is greater than that under slab as impact center.
 307 Therefore, the situation where the pile is the center of impact is the more dangerous. As shown in
 308 Fig. 21, with the increase of impact energy, the displacement value and number of damage failure
 309 units enlarges, which means the structure suffers more damage under CP. Furthermore, the
 310 maximum lateral displacement of pile at the ground surface when $t = 650$ ms, can be calculated by
 311 the following equation:

312

$$S_{mpt} = 0.00934(E + 164.88) = 4.67(mv^2 + 0.33) \quad (3)$$

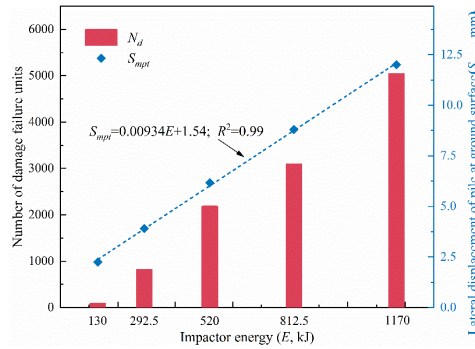


Fig. 21. Dependence of the lateral displacement of 3# pile at the ground surface on impactor energy

313 According to the Chinese Specification for the Design of Rock Retaining Wall Engineering in
 314 Geological Hazards (CAGHP, 2019), the lateral displacement of the resistant sliding pile at the
 315 ground surface must not exceed 10 mm. Substituting this value into Formula 3, the maximum impact
 316 energy that the PSRW can withstand in this study is 905 kJ.

317 *4.3. Comparison with other concrete rockfall retaining walls*

318 Table 6 presents crucial data on an improved cast-in-place rockfall concrete barrier developed
 319 by the US Department of Transportation (Patnaik et al., 2015). This barrier exhibits relatively low
 320 resistance to impact energy, which restricts its applicability to situations where high-impact energy
 321 rockfalls are likely to occur. Integrating a specialized buffering layer on the concrete retaining wall,
 322 the barrier's impact resistance can be effectively enhanced (Kurihashi et al., 2020). According to
 323 Maegawa et al. (2011), concrete rockfall barriers with a buffering layer offer a maximum impact
 324 resistance ranging from approximately 120 to 490 kJ. Addressing the resistance limitations of
 325 traditional concrete rockfall barriers, Furet et al. (2022) proposed the articulated concrete block
 326 rockfall protection structures. These innovative structures allow concrete blocks hingedly connected
 327 to one another, enabling greater impact energy absorption.

328

Table 6 Comparison of different concrete rockfall protection structures

Structure name	The maximum impact energy that structure can withstand (kJ)	Energy dissipation ratio (%)	Interception altitude (m)
Cast-in-place rockfall concrete barriers (Patnaik et al., 2015)	127	/	0.81
Concrete retaining wall with buffering system (Kurihashi et al., 2020)	273	100	2.5
Concrete rock – wall (Maegawa et al., 2011)	490	/	/
Articulated concrete blocks	1020	100	3.2

Note: Energy dissipation ratio denotes the ratio of dissipated energy to input energy.

In terms of energy dissipation, structure damage and friction are responsible for 74% of the impact energy dissipation, with the remaining 26% attributed to other phenomena such as deformation of structural elements, elastic wave propagation, viscous damping, and fracturing. Compared to conventional concrete rockfall barriers, PSRW exhibit significantly higher impact resistance (905 kJ) and interception height (6 m). Similarly, these structures absorb all the impact energy, preventing the impactor from rebounding.

For traditional RC retaining walls subjected to a 16 kJ impact energy, shear cracks develop diagonally from the impact point, with wider spreading observed on the rear face compared to the collision surface (Kurihashi et al., 2020). Fig. 22 illustrates the concrete damage nephogram of PSRW under the impact load of 1170 kN. It is evident that concrete damage primarily concentrated around the impact point and at the junction between the pile and slab. Importantly, there is no evidence of crack penetration into the structure itself, indicating that the PSRW maintains its structural integrity.

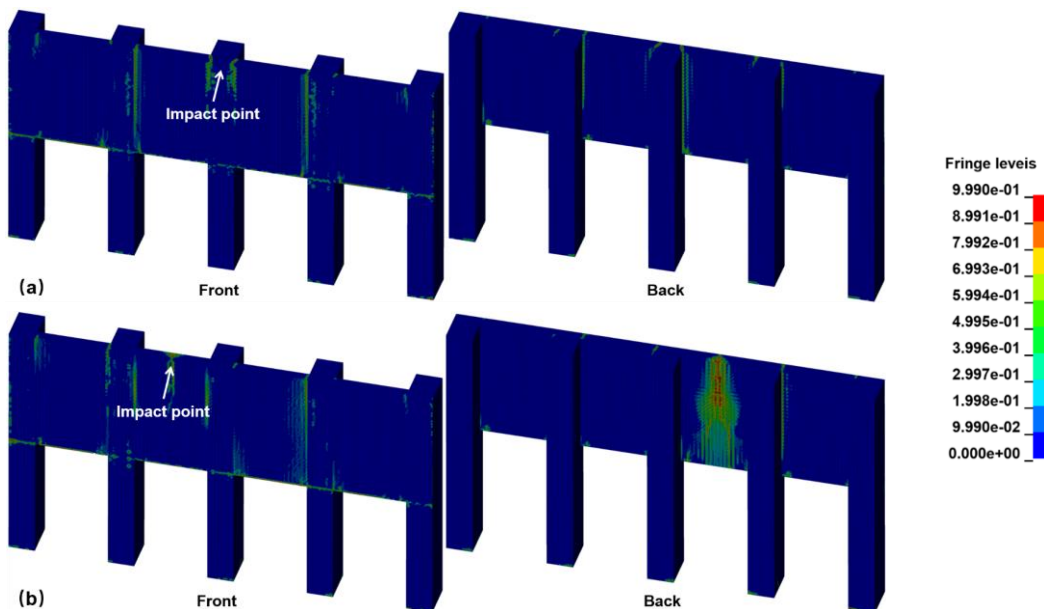


Fig. 22. Damage nephogram of concrete at $t = 650$ ms (a) CP-V30 (b) CS-V30.

Although the lateral displacement of the pile exceeds the stipulated limit, reaching 12 mm as indicated in Table 5 and Figure 21, it is essential to acknowledge that the specified ultimate lateral displacement is frequently a conservative estimation. Concurrently, the maximum lateral displacement at the crown of the cantilever section is 35 mm, which is substantially less than the

347 lateral displacement threshold for the cantilever section of the anti-slide pile. This threshold is
 348 defined as 1% of the cantilever section's length, according to CAGHP (2019). As a result, the impact
 349 load does not compromise the integrity of the structure.

350 In summary, the PSRW is an innovative rockfall protection structure, providing an enhanced
 351 level of impact resistance, increased interception height, and reduced concrete damage. Additionally,
 352 the minimal lateral displacement observed after impact further ensures the structural integrity and
 353 safety in challenging terrain areas.

354 4.4. Discussion on Engineering Practicality

355 The data presented in Table 7 reveal the distribution of rockfall energy levels across four
 356 regions that experience frequent rockfalls. Notably, the Alps region experiences substantial rockfalls,
 357 with many of them exhibiting an impact energy below 1000 kJ. Schneider et al. (2023) utilized
 358 Doppler radar technology to monitor rockfall activity in Brienz/Brinzals, Switzerland. Their
 359 findings indicated that although the volume of rockfalls ranged from 1 to 100 m³, smaller events (1
 360 m³) were markedly more common. As previously mentioned, the PSRW can withstand rockfalls
 361 with an impact energy of about 1000 kJ, making it an ideal solution for a multitude of small alpine
 362 rockfall scenarios. Additionally, its compact size and robust structural stability further enhance its
 363 suitability for mountainous construction projects. In cases where the impact energy of falling rocks
 364 exceeds 1000 kJ, it is advisable to optimize the mechanical properties of the cushion layer, improve
 365 the elastic modulus of concrete, increase the reinforcement ratio of longitudinal tension bars, enlarge
 366 the section size of pile at ground level, or add anchoring measures to enhance the bending resistance
 367 of the retaining structure.

368 **Table 7 Rockfall events in different areas**

Study area	Total number of rockfall events	Rockfall energy < 1000 kJ	Percentage
French Alps (Le Roy et al., 2019)	18	9	50%
Swiss Alps (Dietze et al., 2017)	37	37	100%
Along the railway in Japan (Muraishi et al., 2005)	173	158	91%
New South Wales, Australia (Spadari et al., 2013)	211	200	94%

369 5. Conclusion

370 Compared to existing rockfall protection structures, the PSRW offers enhanced stability and
 371 requires a smaller footprint, making it adept at addressing a broad spectrum of rockfall impact

372 scenarios commonly encountered in alpine canyon regions. In this paper, the dynamic response of
373 the PSRW under different impact centers and velocities were compared and analyzed using the FEM
374 simulation method. Additionally, the influencing factors such as peak impact force, peak interaction
375 force, ratio of peak impact force to peak interaction force, concrete stress, reinforcement stress,
376 maximum lateral displacement of the pile at the ground surface, and ratio of damage failure units to
377 overall structure units were quantified. Notably, the formula for calculating the peak impact force
378 of the PSRW (Eqs. 1), the ratio of peak impact force to peak interaction force (Eqs. 2), maximum
379 lateral displacement of the pile at the ground surface (Eqs. 3) based on the impact energy of rockfalls
380 were proposed. The key findings of this study are as follows:

381 (1) The impact force, interaction force and lateral displacement exhibit a linear correlation with
382 the impact velocity. however, the lateral displacement is more sensitive to velocity variations than
383 the impact force and interaction force.

384 (2) Under different impact centers, the variations in impact force and interaction force are
385 minimal. When the pile serves as the impact center, the lateral displacement of pile at the ground
386 surface and the extent of concrete damage are significantly greater than when the slab center is the
387 impact center. This indicates that impacts centered on the pile pose a more hazardous impact
388 scenario.

389 (3) Concrete damage predominantly concentrates at the joints between piles and slabs, the
390 impact center itself, and the section of piles at the ground surface. To minimize structural concrete
391 damage, it is imperative to prioritize these critical sections in the structural design.

392 (4) The impact force, the ratio of peak impact force to peak interaction force, and the maximum
393 lateral displacement of the pile at the ground surface have a significant correlation with the impact
394 energy. These relationships are crucial for evaluating impact force, interaction force, and the lateral
395 displacement of piles at ground surface during the design of PRSW structures. According to Chinese
396 specifications for displacement requirements, the maximum lateral displacement of the pile at the
397 ground surface should not exceed 10 mm. Consequently, the maximum impact energy that the
398 PSRW can withstand is 905 kJ, when the crown is designated as the impact center.

399 **Data availability**

400 The data that support the findings of this study are available on request from the corresponding

401 author, G Luo, upon reasonable request.

402 **Author contribution**

403 **Peng Zou:** Methodology, Simulation, Visualization, Writing - original draft. **Gang Luo:** Tests
404 design, funding acquisition, writing - review. **Yuzhang Bi:** Visualization, Writing - review. **Hanhua**
405 **Xu:** Writing - review.

406 **Declaration of Competing Interest**

407 The authors declare that they have no known competing financial interests or personal
408 relationships that could have appeared to influence the work reported in this paper.

409 **Acknowledgments**

410 This research was funded by the National Natural Science Foundation of China (42277143),
411 the National Key R&D Program of China (2022YFC3005704), the Sichuan Province Science and
412 Technology Support Program (2024NSFSC0100) and the Science and the research project of the
413 Department of Natural Resources of Sichuan Province (KJ-2023-004, KJ-2023-029). The authors
414 also thank the editors and anonymous reviewers for their constructive comments that improved the
415 manuscript.

416

- 418 Bhatti, A. Q. and Kishi, N.: Impact response of RC rock-shed girder with sand cushion under falling load,
419 Nuclear Engineering and Design, 240, 2626-2632, <https://doi.org/10.1016/j.nucengdes.2010.07.029>,
420 2010.
- 421 Bi, Y., Li, M., Wang, D., Zheng, L., Yan, S., and He, S.: A numerical study of viscous granular flow in
422 artificial step-pool systems: flow characteristics and structure optimization, Acta Geotechnica,
423 <https://doi.org/10.1007/s11440-023-01933-1>, 2023.
- 424 CAGHP: Code for design of rock retaining wall engineering in geological hazards (T/CAGHP060-2019),
425 China University of Geosciences Press, Wuhan 2019. (in Chinese)
- 426 Chau, K. T., Wong, R., and Wu, J.: Coefficient of restitution and rotational motions of rockfall impacts,
427 International Journal of Rock Mechanics and Mining Sciences, 39, 69-77,
428 [https://doi.org/10.1016/S1365-1609\(02\)00016-3](https://doi.org/10.1016/S1365-1609(02)00016-3), 2002.
- 429 Crosta, G. and Agliardi, F.: Parametric evaluation of 3D dispersion of rockfall trajectories, Natural
430 Hazards and Earth System Sciences, 4, 583-598, <https://doi.org/10.5194/nhess-4-583-2004>, 2004.
- 431 Demartino, C., Wu, J. G., and Xiao, Y.: Response of shear-deficient reinforced circular RC columns under
432 lateral impact loading, International Journal of Impact Engineering, 109, 196-213,
433 <https://doi.org/10.1016/j.ijimpeng.2017.06.011>, 2017.
- 434 Dietze, M., Mohadjer, S., Turowski, J. M., Ehlers, T. A., and Hovius, N. J. E. S. D.: Seismic monitoring
435 of small alpine rockfalls—validity, precision and limitations, 5, 653-668, 2017.
- 436 Fan, W., Zhong, Z., Huang, X., Sun, W., and Mao, W.: Multi-platform simulation of reinforced concrete
437 structures under impact loading, Engineering Structures, 266, 114523,
438 <https://doi.org/10.1016/j.engstruct.2022.114523>, 2022.
- 439 Furet, A., Villard, P., Jarrin, J.-P., and Lambert, S.: Experimental and numerical impact responses of an
440 innovative rockfall protection structure made of articulated concrete blocks, Rock Mechanics and
441 Rock Engineering, 55, 5983-6000, <https://doi.org/10.1007/s00603-022-02957-x>, 2022.
- 442 Heng, K., Li, R., Li, Z., and Wu, H.: Dynamic responses of highway bridge subjected to heavy truck
443 impact, Engineering Structures, 232, 11828-11850, <https://doi.org/10.1016/j.engstruct.2020.111828>,
444 2021.
- 445 Hertz, H.: The contact of elastic solids, J Reine Angew, Math, 92, 156-171, 1881.
- 446 Hu, X., Mei, X., Yang, Y., and Luo, G.: Dynamic Response of Pile-plate Rock Retaining Wall under
447 Impact of Rockfall, Journal of Engineering Geology, 27, 123-133, 2019. (in Chinese)
- 448 Hungr, O., Leroueil, S., and Picarelli, L.: The Varnes classification of landslide types, an update,
449 Landslides, 11, 167-194, <https://doi.org/10.1007/s10346-013-0436-y>, 2014.
- 450 Kawahara, S. and Muro, T.: Effects of dry density and thickness of sandy soil on impact response due to
451 rockfall, Journal of terramechanics, 43, 329-340, <https://doi.org/10.1016/j.jterra.2005.05.009>, 2006.
- 452 Kurihashi, Y., Oyama, R., Komuro, M., Murata, Y., and Watanabe, S.: Experimental study on buffering
453 system for concrete retaining walls using geocell filled with single-grain crushed stone,
454 International Journal of Civil Engineering, 18, 1097-1111, <https://doi.org/10.1007/s40999-020-00520-9>, 2020.
- 456 Labiouse, V., Descoedres, F., and Montani, S.: Experimental study of rock sheds impacted by rock
457 blocks, Structural Engineering International, 6, 171-176,
458 <https://doi.org/10.2749/101686696780495536>, 1996.
- 459 Lambert, S., Gotteland, P., and Nicot, F.: Experimental study of the impact response of geocells as

460 components of rockfall protection embankments, *Natural Hazards and Earth System Sciences*, 9,
461 459-467, <https://doi.org/10.5194/nhess-9-459-2009>, 2009.

462 Le Roy, G., Helmstetter, A., Amitrano, D., Guyoton, F., and Le Roux-Mallouf, R.: Seismic analysis of
463 the detachment and impact phases of a rockfall and application for estimating rockfall volume and
464 free-fall height, 124, 2602-2622, <https://doi.org/10.1029/2019JF004999>, 2019.

465 Lee, K., Chang, N., and Ko, H.: Numerical simulation of geosynthetic-reinforced soil walls under seismic
466 shaking, *Geotextiles and Geomembranes*, 28, 317-334,
467 <https://doi.org/10.1016/j.geotexmem.2009.09.008>, 2010.

468 Lu, L., Lin, H., Wang, Z., Xiao, L., Ma, S., and Arai, K.: Experimental and numerical investigations of
469 reinforced soil wall subjected to impact loading, *Rock Mechanics and Rock Engineering*, 54, 5651-
470 5666, <https://doi.org/10.1007/s00603-021-02579-9>, 2021.

471 Maegawa, K., Yokota, T., and Van, P. T.: Experiments on rockfall protection embankments with geogrids
472 and cushions, *GEOMATE Journal*, 1, 19-24, 2011.

473 Mavrouli, O., Giannopoulos, P., Carbonell, J. M., and Syrmakezis, C.: Damage analysis of masonry
474 structures subjected to rockfalls, *Landslides*, 14, 891-904, <https://doi.org/10.1007/s10346-016-0765-8>, 2017.

476 Muraishi, H., Samizo, M., and Sugiyama, T.: Development of a flexible low-energy rockfall protection
477 fence, *Quarterly Report of RTRI*, 46, 161-166, <https://doi.org/10.2219/rtriqr.46.161>, 2005.

478 Patnaik, A., Musa, A., Marchetty, S., and Liang, R.: Full-scale testing and performance evaluation of
479 rockfall concrete barriers, *Transportation research record*, 2522, 27-36,
480 <https://doi.org/10.3141/2522-03>, 2015.

481 Peila, D. and Ronco, C.: Design of rockfall net fences and the new ETAG 027 European guideline,
482 *Natural Hazards and Earth System Sciences*, 9, 1291-1298, <https://doi.org/10.5194/nhess-9-1291-2009>, 2009.

484 Peila, D., Oggeri, C., and Castiglia, C.: Ground reinforced embankments for rockfall protection: design
485 and evaluation of full scale tests, *Landslides*, 4, 255-265, <https://doi.org/10.1007/s10346-007-0081-4>, 2007.

487 Perera, J. S., Lam, N., Disfani, M. M., and Gad, E.: Experimental and analytical investigation of a RC
488 wall with a gabion cushion subjected to boulder impact, *International Journal of Impact Engineering*,
489 151, 103823-103839, <https://doi.org/10.1016/j.ijimpeng.2021.103823>, 2021.

490 Pichler, B., Hellmich, C., Mang, H. A., and Eberhardsteiner, J.: Loading of a gravel-buried steel pipe
491 subjected to rockfall, *Journal of Geotechnical and Geoenvironmental Engineering*, 132, 1465-1473,
492 [https://doi.org/10.1061/\(ASCE\)1090-0241\(2006\)132:11\(1465\)](https://doi.org/10.1061/(ASCE)1090-0241(2006)132:11(1465)), 2006.

493 Schellenberg, K.: On the design of rockfall protection galleries, *ETH Zurich*, 2008.

494 Schneider, M., Oestreicher, N., Ehrat, T., and Loew, S.: Rockfall monitoring with a Doppler radar on an
495 active rockslide complex in Brienz/Brinzauls (Switzerland), 23, 3337-3354,
496 <https://doi.org/10.5194/nhess-23-3337-2023>, 2023.

497 Shen, W., Zhao, T., Dai, F., Jiang, M., and Zhou, G. G.: DEM analyses of rock block shape effect on the
498 response of rockfall impact against a soil buffering layer, *Engineering Geology*, 249, 60-70,
499 <https://doi.org/10.1016/j.enggeo.2018.12.011>, 2019.

500 Spadari, M., Kardani, M., De Carteret, R., Giacomini, A., Buzzi, O., Fityus, S., and Sloan, S.: Statistical
501 evaluation of rockfall energy ranges for different geological settings of New South Wales, Australia,
502 158, 57-65, <https://doi.org/10.1016/j.enggeo.2013.03.007>, 2013.

503 Tian Y., Luo G., Zou P., Zhang L., Hou Y.: Study on design method of rockfall retaining pile under

504 rockfall impact, 35, 88-96, <https://doi.org/10.16031/j.cnki.issn.1003-8035.202304026>, 2024. (in
505 Chinese)

506 Truong, P. and Lehane, B.: Effects of pile shape and pile end condition on the lateral response of
507 displacement piles in soft clay, *Géotechnique*, 68, 794-804, <https://doi.org/10.1680/jgeot.16.P.291>,
508 2018.

509 Volkwein, A., Schellenberg, K., Labiouse, V., Agliardi, F., Berger, F., Bourrier, F., Dorren, L. K., Gerber,
510 W., and Jaboyedoff, M.: Rockfall characterisation and structural protection—a review, *Natural
511 Hazards and Earth System Sciences*, 11, 2617-2651, <https://doi.org/10.5194/nhess-11-2617-2011>,
512 2011.

513 Wu, J., Ma, G., Zhou, Z., Mei, X., and Hu, X.: Experimental Investigation of Impact Response of RC
514 Slabs with a Sandy Soil Cushion Layer, *Advances in Civil Engineering*, 1-18,
515 <https://doi.org/10.1155/2021/1562158>, 2021.

516 Yang, J., Duan, S., Li, Q., and Liu, C.: A review of flexible protection in rockfall protection, *Natural
517 Hazards*, 99, 71-89, <https://doi.org/10.1007/s11069-019-03709-x>, 2019.

518 Yong, A. C., Lam, N. T., and Menegon, S. J.: Closed-form expressions for improved impact resistant
519 design of reinforced concrete beams, *Structures*, 29, 1828-1836,
520 <https://doi.org/10.1016/j.istruc.2020.12.041>, 2021.

521 Yong, A. C., Lam, N. T., Menegon, S. J., and Gad, E. F.: Experimental and analytical assessment of
522 flexural behavior of cantilevered RC walls subjected to impact actions, *Journal of Structural
523 Engineering*, 146, 04020034, [https://doi.org/10.1061/\(ASCE\)ST.1943-541X.0002578](https://doi.org/10.1061/(ASCE)ST.1943-541X.0002578), 2020.

524 Yu, Z., Luo, L., Liu, C., Guo, L., Qi, X., and Zhao, L.: Dynamic response of flexible rockfall barriers
525 with different block shapes, *Landslides*, 18, 2621-2637, [https://doi.org/10.1007/s10346-021-01658-
526 w](https://doi.org/10.1007/s10346-021-01658-w), 2021.

527 Zhao, P., Xie, L., Li, L., Liu, Q., and Yuan, S.: Large-scale rockfall impact experiments on a RC rock-
528 shed with a newly proposed cushion layer composed of sand and EPE, *Engineering Structures*, 175,
529 386-398, <https://doi.org/10.1016/j.engstruct.2018.08.046>, 2018.

530 Zhong, H., Lyu, L., Yu, Z., and Liu, C.: Study on mechanical behavior of rockfall impacts on a shed slab
531 based on experiment and SPH-FEM coupled method, *Structures*, 33, 1283-1298,
532 <https://doi.org/10.1016/j.istruc.2021.05.021>, 2021.

533 Zhong, H., Yu, Z., Zhang, C., Lyu, L., and Zhao, L.: Dynamic mechanical responses of reinforced
534 concrete pier to debris avalanche impact based on the DEM-FEM coupled method, *International
535 Journal of Impact Engineering*, 167, 104282-104301,
536 <https://doi.org/10.1016/j.ijimpeng.2022.104282>, 2022.